Pergamon

Int. J. Heat Mass Transfer. Vol. 38, No. 9, pp. 1647–1659, 1995
Copyright © 1995 Elsevier Science Ltd
Printed in Great Britain. All rights reserved
0017-9310/95 $9.50+0.00

0017-9310(94)00294-0

Melting and solidification of thin wires: a class of phase-change problems with a mobile interface—II. Experimental confirmation

I. M. COHEN, L. J. HUANG† and P. S. AYYASWAMY‡

Department of Mechanical Engineering and Applied Mechanics, University of Pennsylvania, Philadelphia, PA 19104-6315, U.S.A.

(*Received* 24 *March* 1994 *and in final form* 11 *August* 1994)

Abstract—In Part I, we formulated the problem of wire heating, melting, roll-up into a ball, cooling and solidification. In this part, we describe experimental observations of the melting and solidification processes using high speed photography in an arc chamber. These observations provide results for comparison with the theoretical model. In the numerical computations for the theoretical model, the heat flux from the arc plasma to the wire is an input parameter. The value of this heat flux is obtained from temperature measurements made by thermocouples embedded in the unmelted wire above the ball, thus enabling comparisons between the predictions of the theoretical model and experimental observations. The heat transfer results indicate that conduction up the wire, for thin wires, is the dominant mechanism; the solidification front in the melt progresses from top downwards. The models described in Parts I and II have many applications apart from demonstrating suitable analytical and numerical procedures for treating phase-change problems with moving interfaces. The most important practical application is in semiconductor chip assembly and packaging by the ball bonding process.

1. EXPERIMENTAL PROCEDURE

Aluminum and copper melts were formed from thin wires in a partially evacuated arc chamber, and the corresponding current, voltage, pressure and temperature values were recorded. The sequences were photographed for subsequent examination.

The melts were produced in an arc chamber described in Cohen *et al.* [1] and Huang *et al.* [2]. Briefly, the arc chamber is constructed of two concentric circular cylinders of stainless steel tubing approximately 0.3 m (1 ft) high. There are four observation ports 90° apart on the central plane of the chamber, two with glass windows. One port has a T-fitting, which is connected to the vacuum pump and to a needle valve that can be connected to a gas bottle. Another port is fitted with a U-tube, mercury-filled vacuum gauge. Wilson-type seals pass the electrode holders at the top and bottom into the chamber and seal it for both pressure and vacuum. The electrodes consist of a pair of hollow, threaded copper cylinders. Into one end of the bottom cylinder a 1% thoriated tungsten flat electrode tip is inserted, while the other end screws onto the electrode holder. In the top electrode, a 12.7 mm (0.5 in.) aluminum plug replaces the thoriated tungsten tip. A hole is drilled through the center of this plug to accomodate the wire sample. The chamber is connected to a Welch Model 1397 mechanical vacuum pump and can evacuate the arc chamber to approximately 0.01 atm within a few minutes. A 40 kW Thermal Dynamics plasma flame d.c. power supply provides 90 V open-circuit d.c. output with full-wave rectification from 480 V, three-phase, 60 Hz a.c. An LC filter reduces the output ripple to less than 2%, and the dominant frequency is 360 Hz. A ballast resistor is placed in the circuit to control and vary the current through the electrical discharge. Ignition is achieved by bringing the wire and the bottom electrode in contact with each other, allowing current to flow, and then raising the wire pneumatically (with two compressed air cylinders) to a predetermined gap setting. The arc is drawn out and remains conducting at a current determined by an adjustable ballast resistor until it is extinguished by terminating the power supply. Figure 1 shows the general configuration.

In the experiments, an IBM PC-AT with a Data Translation 2801A data acquisition board and DT 707 terminal board were used for recording data. This was supported by ASYSTANT+software for the data management, manipulation, and display. A nominal 10 mΩ shunt resistor (actually 0.00949 Ω) was placed in series with the arc current and a 1 MΩ/13 KΩ voltage divider was placed in parallel with the arc voltage to reduce both signals to voltages that can be accepted by the DT 2801A. Pressure was measured by an MKS Barotron model 122A transducer. Temperature was measured by 0.127 mm diameter type K (chromel–alumel) thermocouples implanted in 0.33 mm diameter holes drilled in the wire. The ther-

† Harrison Radiator, Division of General Motors Corporation, Lockport, NY 14094-1896, U.S.A.

‡ Author to whom correspondence should be addressed.

NOMENCLATURE

c_p	specific heat [J kg^{-1} K^{-1}]
h	heat transfer coefficient [W m^{-2} K^{-1}], lengths (denoted by subscripts)
k	thermal conductivity [W m^{-1} K^{-1}]
I	current [A]
p	pressure [Pa]
q	heat flux [W m^{-2}]
Q	total heat [W]
S_b	surface area of the ball formed
t	time
T	temperature [K]
V	voltage [V].

Greek symbols

ε	emissivity
λ	latent heat
$\hat{\sigma}$	Stefan–Boltzmann constant [W m^{-2} K^{-4}].

Subscripts

a	ambient
av	average
g	gap
m	melting condition
o	initial condition
w	wire.

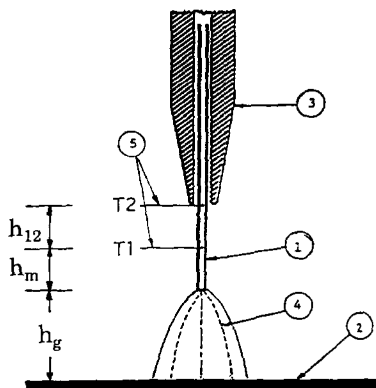

1. wire electrode
2. wand electrode
3. ceramic capillary
4. electric discharge
5. thermocouples

Fig. 1. Schematic of the experiment for temperature measurement.

mocouples were held in place by high temperature cement after being coated with a special insulating lacquer (see Fig. 1). Because the thermocouple wires were so fragile and were so close to the arc, they were further protected from melting by ceramic capillaries. Arc current, voltage, pressure and wire temperatures were recorded simultaneously. Timing circuits and relays allowed the entire sequence, i.e. from electrode short circuit to ignition, pneumatic electrode separation, arc and termination of current, to be pre-programmed on the computer. Each interval was set to insure proper operation. The arc duration was variable and was pre-set. The parameters used in the discharge were chosen to provide a greatly enlarged and slowed down version of ball formation in the microelectronic packaging process of wire bonding (Cohen and Ayyaswamy [3]). The dimensionless parameter that is kept invariant in the modeling is $I\Delta V\Delta t/(ph_{go}^3)$, where I is the current through the discharge, ΔV is the voltage drop between the electrodes, Δt is the duration, p is the pressure and h_{go} is the initial gap length between the wire tip and the planar electrode (wand). We scale the current up by 30 ×, the voltage drop down by 10 ×, the time up by 100 ×, the pressure down by 50 × and the gap length up by 50 × (approximately), compared with the process on the real wire bonding scale.

We used a Hycam II, 16 mm high speed rotating prism camera with Kodak 7250 high speed Tungsten Ektachrome Video News Film. The camera has the capability to run from 10 to 11 000 full frames s^{-1}. After the arc was extinguished, the melt was externally illuminated by a DP Lowell 1000 W quartz–halogen lamp through the glass in one of the four ports. The melting and solidification processes were satisfactorily resolved at 500 frames s^{-1}. We typically used 30.48 m spools of film which, at 500 frames s^{-1}, provided 8 s of running time.

2. RESULTS AND DISCUSSION

Figures 2(a)–8(a) are a sequence of photographs from a high speed film of a run made in air with 0.9999 purity copper. Figures 2(a) and 3(a) are pictures of the melting process. After a small part of the wire had been melted [Fig. 2(a)], the pendant drop hung from the bottom of the unmelted portion of the wire. With a larger part of the wire melted [Fig. 3(a)], the melt elongated towards the wire tip due to gravity and surface tension gradient. At the termination of the discharge, a fully formed molten ball is seen in Fig. 4(a). A sequence of photographs during the sol-

Fig. 2(a). One frame of the high speed cinematography of the ball during melting in air, $R_w = 0.8$ mm, $p = 18$ mmHg, 0.9999 copper anode.

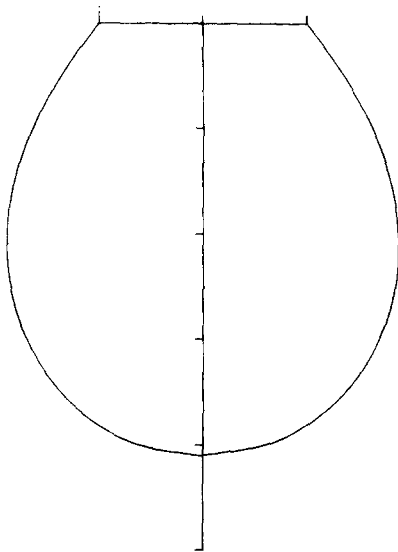

Fig. 2(b). The ball corresponding to Fig. 2(a) generated by solving equation (23) of Part I [4].

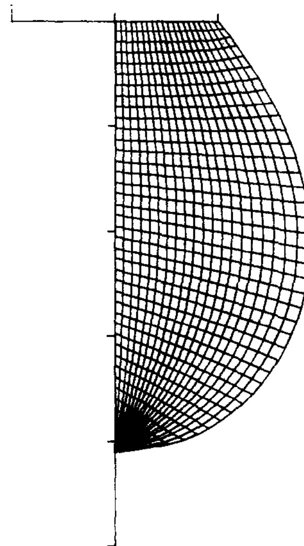

Fig. 2(c). The body-fitted coordinate system corresponding to Fig. 2(b) generated by equations (54) and (55) of Part I [4].

idification process is displayed in Figs. 5(a)–8(a). The solid–liquid interface movement is from the neck to the bottom of the ball. This suggests that during the solidification process, the heat flow from the molten ball is predominantly due to conduction up the wire, and losses due to convection and radiation from the ball surface to the ambient appear small by comparison. A fully solidified ball is shown in Fig. 8(a).

Figures 2(b)–8(b) are the predictions of the instantaneous melt shapes and the locations of the solid–liquid interface from our analytical/numerical modeling for conditions identical to those of the experiments [Figs. 2(a)–8(a)]. These have been generated by solving equation (30) of Part I, which includes the effects of gravity and surface tension gradient. For identical conditions, the predictions of our analytical/numerical technique agree remarkably well with the photographs.

Figures 2(c)–8(c) show the corresponding grid and solid–liquid interface movement using the body-fitted

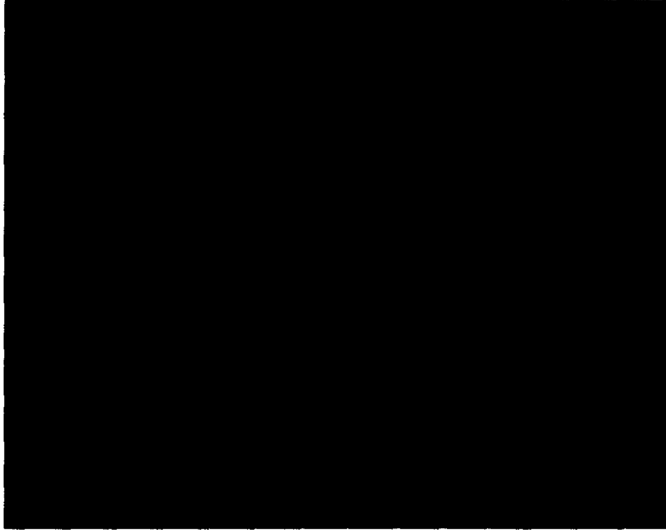

Fig. 3(a). One frame of the high speed cinematography of the ball during melting in air, $R_w = 0.8$ mm, $p = 18$ mmHg, 0.9999 copper anode.

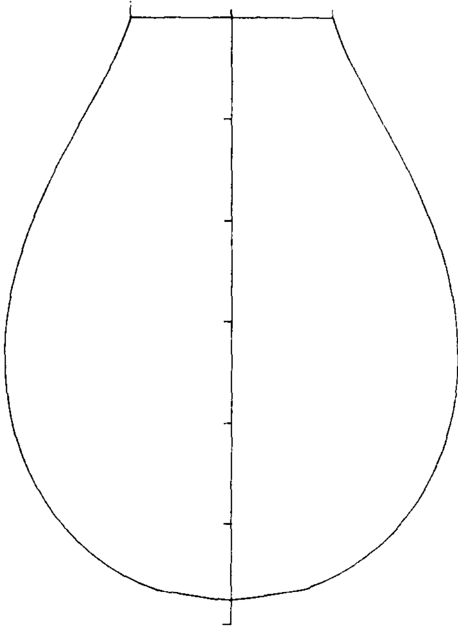

Fig. 3(b). The ball corresponding to Fig. 3(a) generated by solving equation (23) of Part I [4].

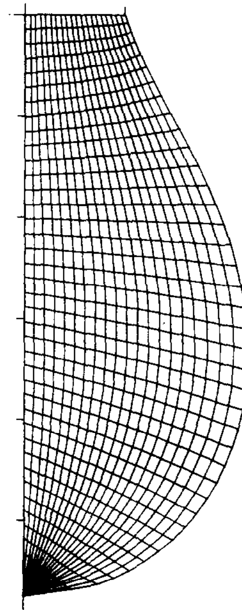

Fig. 3(c). The body-fitted coordinate system corresponding to Fig. 3(b) generated by equations (54) and (55) of Part I [4].

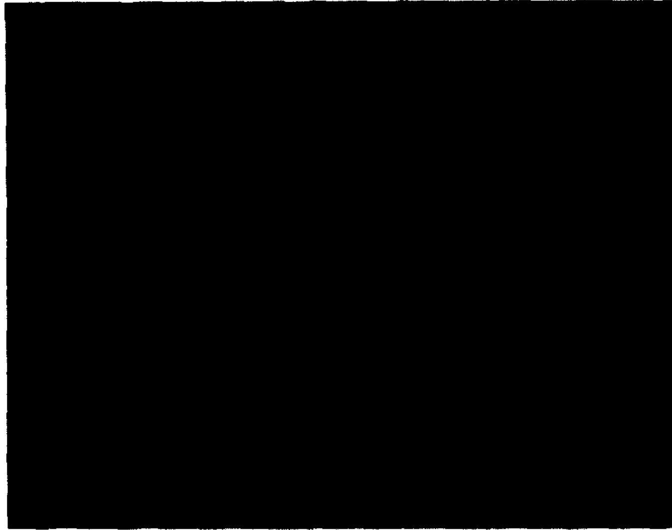

Fig. 4(a). One frame of the high speed cinematography of the ball at arc termination in air, $R_w = 0.8$ mm, $p = 18$ mmHg, 0.9999 copper anode.

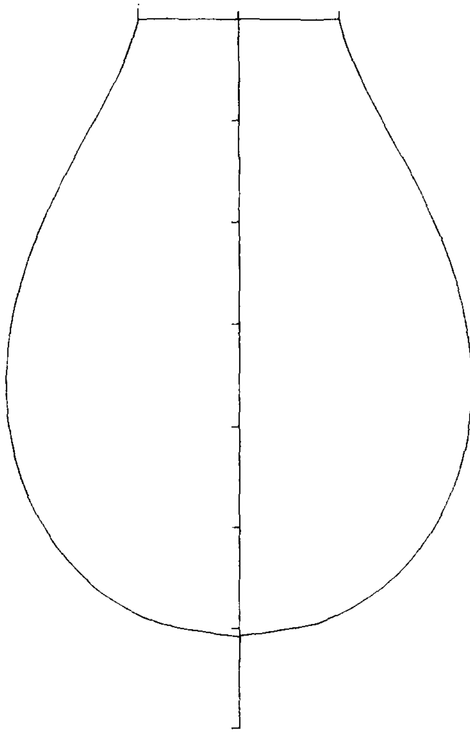

Fig. 4(b). The ball corresponding to Fig. 4(a) generated by solving equation (23) of Part I [4].

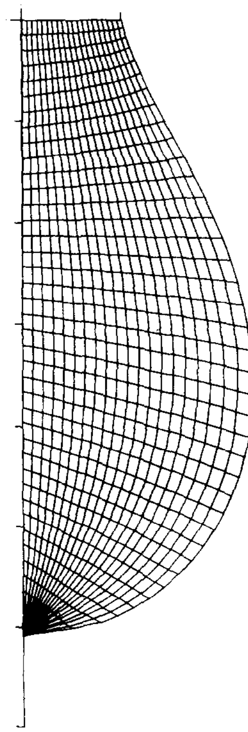

Fig. 4(c). The body-fitted coordinate system corresponding to Fig. 4(b) generated by equations (54) and (55) of Part I [4].

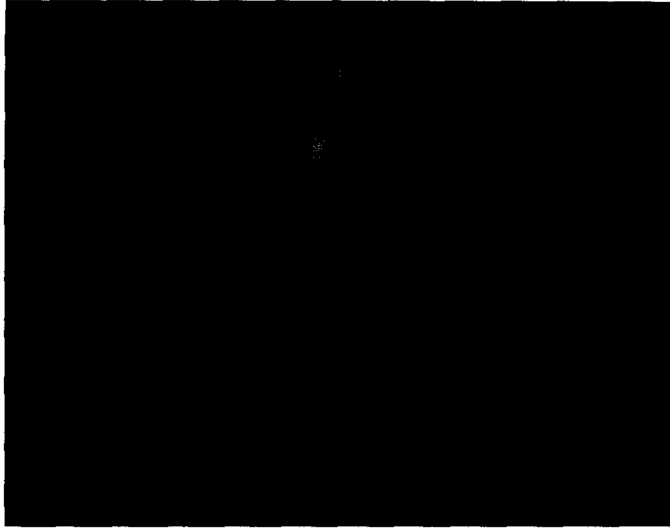

Fig. 5(a). One frame of the high speed cinematography of the ball during the solidification process in air, $R_w = 0.8$ mm, $p = 18$ mmHg, 0.9999 copper anode.

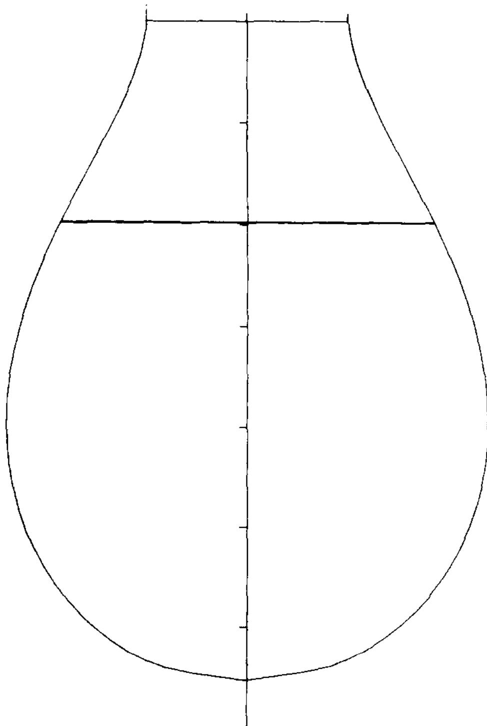

Fig. 5(b). The ball corresponding to Fig. 5(a) generated by solving equation (23) of Part I [4].

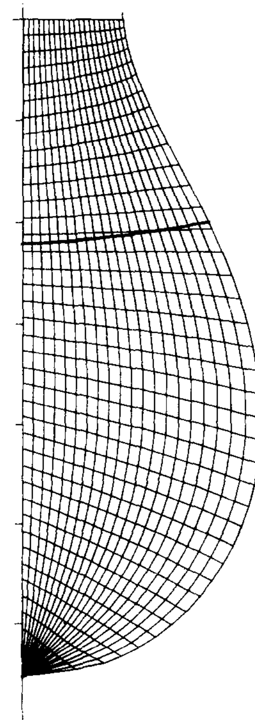

Fig. 5(c). The body-fitted coordinate system corresponding to Fig. 5(b) generated by equations (54) and (55) of Part I [4].

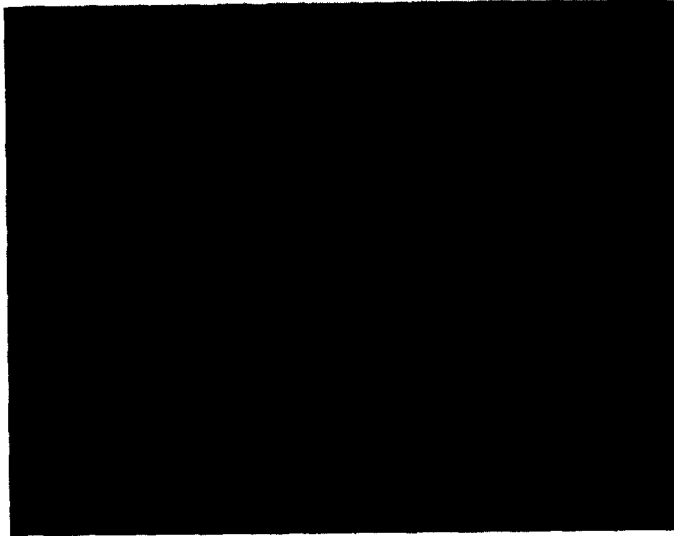

Fig. 6(a). One frame of the high speed cinematography of the ball during the solidification process in air. $R_w = 0.8$ mm, $p = 18$ mmHg, 0.9999 copper anode.

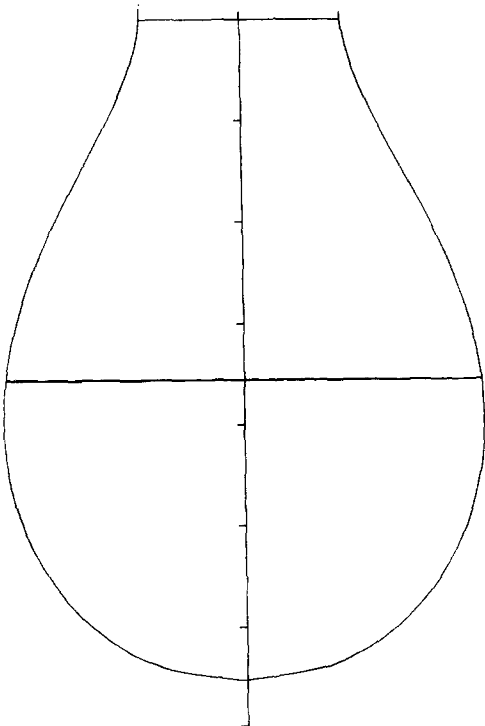

Fig. 6(b). The ball corresponding to Fig. 6(a) generated by solving equation (23) of Part I [4].

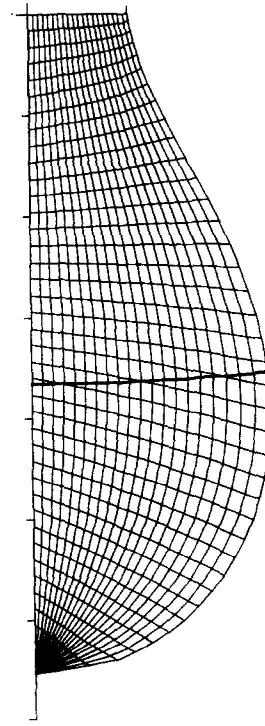

Fig. 6(c). The body-fitted coordinate system corresponding to Fig. 6(b) generated by equations (54) and (55) of Part I [4].

Fig. 7(a). One frame of the high speed cinematography of the ball during the solidification process in air, $R_w = 0.8$ mm, $p = 18$ mmHg, 0.9999 copper anode.

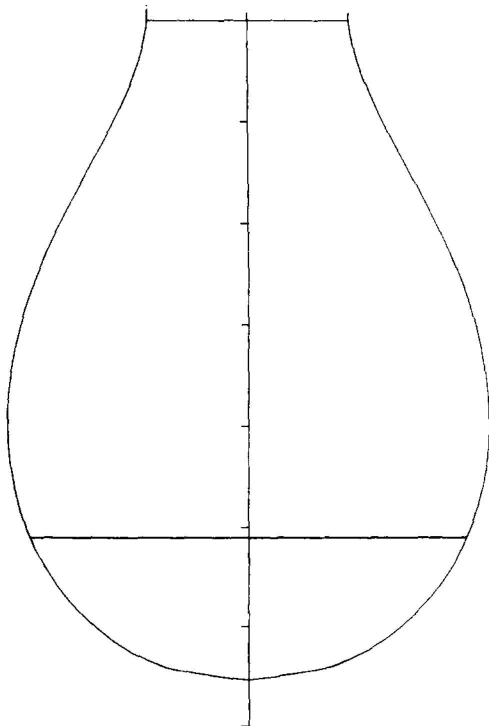

Fig. 7(b). The ball corresponding to Fig. 7(a) generated by solving equation (23) of Part I [4].

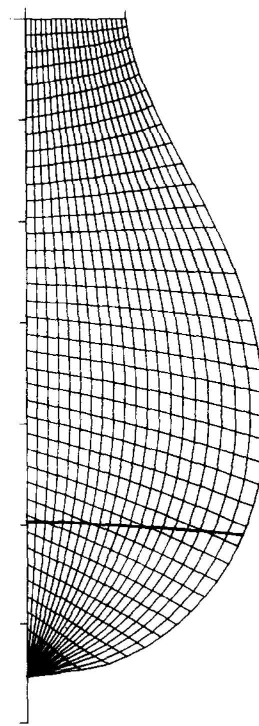

Fig. 7(c). The body-fitted coordinate system corresponding to Fig. 7(b) generated by equations (54) and (55) of Part I [4].

Fig. 8(a). One frame of the high speed cinematography of the ball during the solidification process in air, $R_w = 0.8$ mm, $p = 18$ mmHg, 0.9999 copper anode.

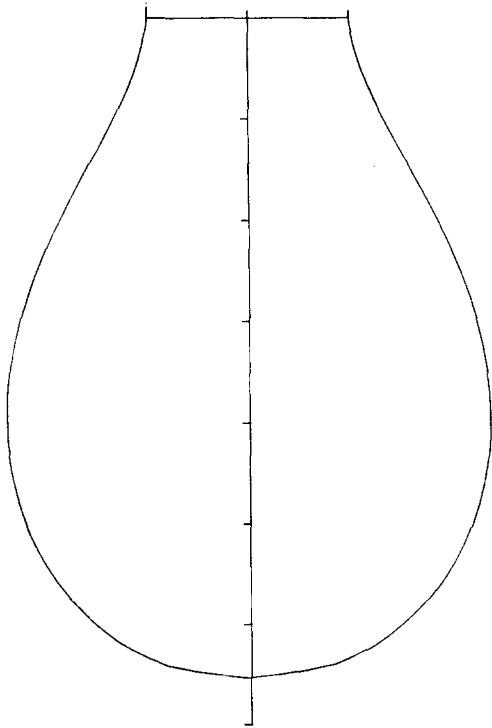

Fig. 8(b). The ball corresponding to Fig. 8(a) generated by solving equation (23) of Part I [4].

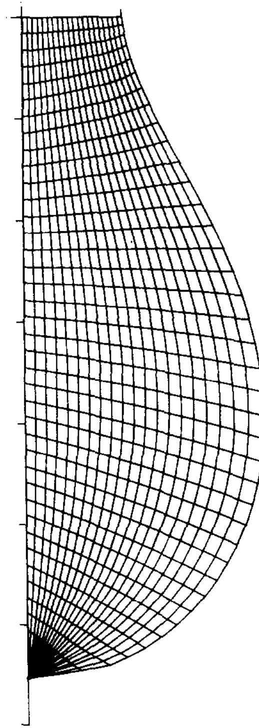

Fig. 8(c). The body-fitted coordinate system corresponding to Fig. 8(b) generated by equations (54) and (55) of Part I [4].

coordinate system, and have been included to display the numerical evaluation. The results show that the solidification front progresses downwards with time.

In Fig. 9, the temperature responses T1 and T2 of the thermocouples (see Fig. 1) are shown. The discharge was in air at a pressure $p = 2.4 \times 10^3$ Pa (18 mmHg); the ballast resistance was 2.5 Ω. Pure aluminum wire (3.2 mm diameter) was the cathode. When the wire and bottom electrodes were in contact, the short-circuit current was 35.6 A. At $t = 5.25$ s, the wire was raised and an arc was drawn out. The initial gap between the wire and bottom electrode was 8 mm. The arc current was about 21 A and $\Delta V = 38$ V. The arc was maintained at these values for a period of 2.75 s to cause (a) heating and melting of the wire and (b) roll up of the melt to form a ball. A wire length of 4 mm was consumed in the process. The arc was extinguished at $t = 8$ s, and the melt was allowed to cool by conduction up the wire, and radiation and natural convection from the lateral surfaces of the wire and the melt. Thermocouple T1 senses wire heating from $t = 5.25$ s to $t = 8.00$ s, and then cooling followed by solidification. For thermocouple T2, the time responses are the same; however the heat conduction resistance of the wire length between T1 and T2, (h_{12} in Fig. 1), reduces the temperature level. The simultaneous temperature profiles T1 and T2 enable us to pose the inverse heat transfer problem and predict the average heat flux delivered to the wire tip during the entire melting and solidification processes. This calculation is illustrated below.

2.1. *Calculation of the heat flux*

This discussion is with reference to the sample data shown in Fig. 9. Consider the heating period during which the arc is present and heat is supplied to cause melting and roll up of the segment of wire between the tip and the location of the first thermocouple T1 (see Fig. 1). Let the duration of this heating be denoted by Δt and the length of this melted segment be h_m. We now demonstrate how the approximate magnitude of

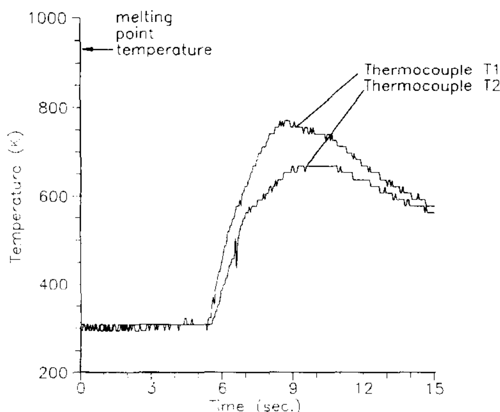

Fig. 9. Temperatures of the thermocouples T1 and T2 with time, discharge in air, $R_w = 1.59$ mm, $p = 18$ mmHg, 0.99999 aluminum cathode.

the average heat flux supplied by the arc to the wire during this process may be evaluated. Consider an energy balance applicable for Δt that is based on average heat flux quantities. This yields

$$q_{av} = q_{1,av} + q_{2,av} + q_{3,av} + q_{4,av} \tag{1}$$

where q_{av} is the total average heat flux supplied during Δt, $q_{1,av}$ is the heat flux conducted up the wire normal to the wire cross section, $q_{2,av}$ is the sensible heat flux imparted to the segment h_m causing its temperature to rise from an initial wire temperature to the final temperature at the end of heating $\Delta(t)$, $q_{3,av}$ is the latent heat flux required to melt the wire segment h_m at the melting temperature of the wire material and $q_{4,av}$ is the heat flux lost by radiation and convection from the ball surface formed by roll up. The various average flux quantities may in turn be expressed as follows:

$$q_{1,av} = k_{av} \Delta T_{12,av} / h_{12} \tag{2}$$

where k_{av} is the average thermal conductivity of the wire material during Δt, $\Delta T_{12,av}$ is the average temperature difference between the thermocouple readings T1 and T2, and h_{12} is the distance between the thermocouple locations (see Fig. 1).

$$q_{2,av} = \rho c_p (\Delta T / \Delta t) h_m \tag{3}$$

where ΔT is the temperature difference between the final and initial temperatures of the wire.

$$q_{3,av} = \rho \lambda h_m / \Delta t \tag{4}$$

where λ is the latent heat for melting, and

$$q_{4,av} = S_b [h(T - T_a) + \varepsilon \hat{\sigma} (T^4 - T_a^4)] / \pi R_w^2 \tag{5}$$

where S_b is the surface area of the ball formed by roll up. The total average energy input to the wire during Δt would be given by

$$Q_w = q_{av} \pi R_w^2. \tag{6}$$

The total energy of the arc is given by

$$Q_{arc} = I \Delta V \Delta t \text{ J} \tag{7}$$

where I is current and ΔV is the voltage difference.

For the particular situation displayed in Fig. 9, with thin aluminum wire used as cathode, $h_m = 4$ mm, $\Delta t = (8-5.25) = 2.75$ s, $q_{1,av} = 7.2 \times 10^6$ W m^{-2}, $q_{2,av} = 3.69 \times 10^6$ W m^{-2}, $q_{3,av} = 2.58 \times 10^6$ W m^{-2}, $q_{4,av} = 5.8 \times 10^4$ W m^{-2}, giving a value for $q_{av} = 1.35 \times 10^7$ W m^{-2}. The wire radius $R_w = 1.6$ mm, $Q_w = 292.4$ J, $I = 21$ A, $\Delta V = 38$ V, giving a value for $Q_{arc} = 2249$ J. The fraction of the total energy transferred to the wire is $Q_w / Q_{arc} = 0.13$.

Figures 10 and 11 show the timewise temperature traces for T1 and T2 calculated from the numerical model and their comparison with experimental measurements. The agreement is excellent. The ability of the numerical model to closely mimic the temperature traces is interpreted as justification of its veracity and utility.

Both our numerical and experimental studies of

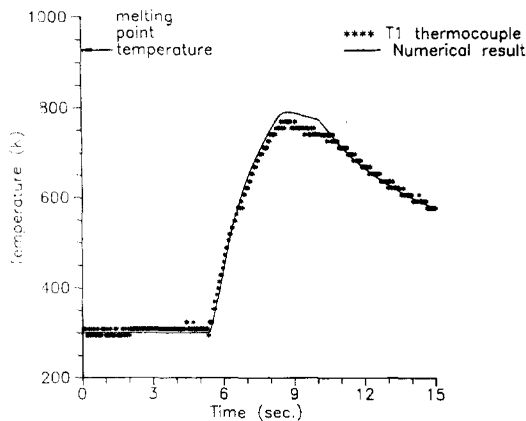

Fig. 10. Comparison of temperature T1 with numerical result, discharge in air, $R_w = 1.59$ mm, $p = 18$ mmHg, 0.99999 aluminum cathode.

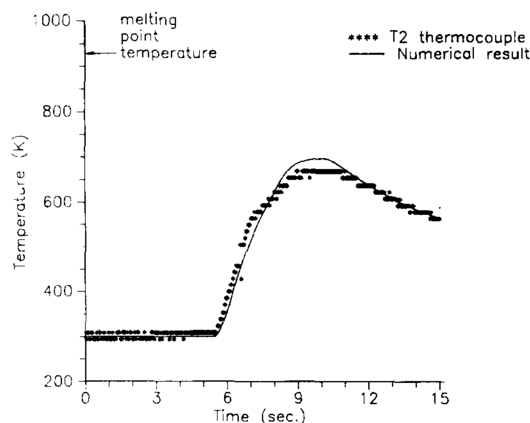

Fig. 11. Comparison of temperature T2 with numerical result, discharge in air, $R_w = 1.59$ mm, $p = 18$ mmHg, 0.99999 aluminum cathode.

the solidification process have shown that voids may appear inside the melt due to shrinkage associated with the density difference between liquid and solid phases. We note that with the presence of voids, the minimum energy principle {equations (14) and (15) of Part I [4]} has to be suitably modified to reflect the presence of a growing void and the associated changes of liquid and void volumes and surface energies. In the numerical scheme, the solution is started off with a microbubble positioned at the centroid of the melt and is allowed to evolve in space and time. Figures 12 and 13 show a sectioned ball with a void in it and a numerical solution simulating such a circumstance. Detailed discussions of these features are provided elsewhere (see Cohen *et al.* [1] and Huang *et al.* [5]). In [5], we compared the final configurations at the end of the solidification process for pure aluminum with those for an aluminum–silicon alloy. In the pure aluminum, a shrinkage void occupying as much as 12% of the initial melt volume may occur. The alloy composition is such that solidification occurs over a range of 19 K. The void fraction is $2.2 \times 10^{-4}\%$. In general, for identical conditions, a smaller void volume results with the alloy than with pure metal. This may be explained in terms of the temperature drop in the liquid and mushy regions. The maximum temperature drop (between the void–liquid interface and the outer surface of the ball) is noted to be less than 2 K, whereas the temperature range of solidification, ΔT_{LS}, happens to be between 11 K and 20 K. Because of this, at the beginning of solidification, only liquid and mushy regions exist in the melt. The completely solidified region appears in the system at a much later time than with the pure metal case. At this point, only the mush and solid regions exist. The void begins to grow coincident with the appearance of the solid region. These many factors appear to contribute to a smaller void when an alloying element is present. We note that none of this discussion applies to very large voids which we have found in some balls and attribute to vaporization.

In all of these numerical calculations, the relative error is less than 0.2% and the absolute error is less than 10^{-7}.

3. SUMMARY AND CONCLUSIONS

The following conclusions may be drawn from this study in the case when a wire is heated from below.

(1) For wire diameters less than about 10^{-3} m, molten metal such as copper may roll up to form a spherical ball since the surface tension is dominant.

(2) The effects of both (i) gravity and (ii) variation in the surface tension due to temperature gradients are such as to elongate the ball.

(3) The time taken for the initial heat-up period is very short compared to that required for the melting processes.

(4) During normal heating, the maximum temperature in the melt is located near the bottom surface and is lower than the boiling temperature.

(5) The dominant heat loss mechanism is conduction up the wire. Solidification proceeds from the top (wire) downwards.

(6) Shrinkage voids in alloys are smaller than those in pure metals because solidification occurs over a range of temperatures.

(7) The numerical values of heat fluxes deduced from the upscaled temperature measurements permitted a complete numerical simulation which followed the experimental data very well.

Acknowledgements—The authors gratefully acknowledge support of their work by NSF under grant DMC 8709537, by the Benjamin Franklin Technology Center of Southeastern Pennsylvania under Benjamin Franklin Partnership grant 07.510 RU, and by the International Society for Hybrid Microelectronics–Educational Foundation under grants 88-13 and 89-006C. They remain indebted to Mr Lee Levine of Kulicke and Soffa Industries, Inc. for his advice and for arranging the donation of K & S bonding machinery and to Johnson-Matthey Electronics for the donation of specially prepared wire samples. They are grateful to the Pittsburg Supercomputing Center for the use of the CRAY Y-MP.

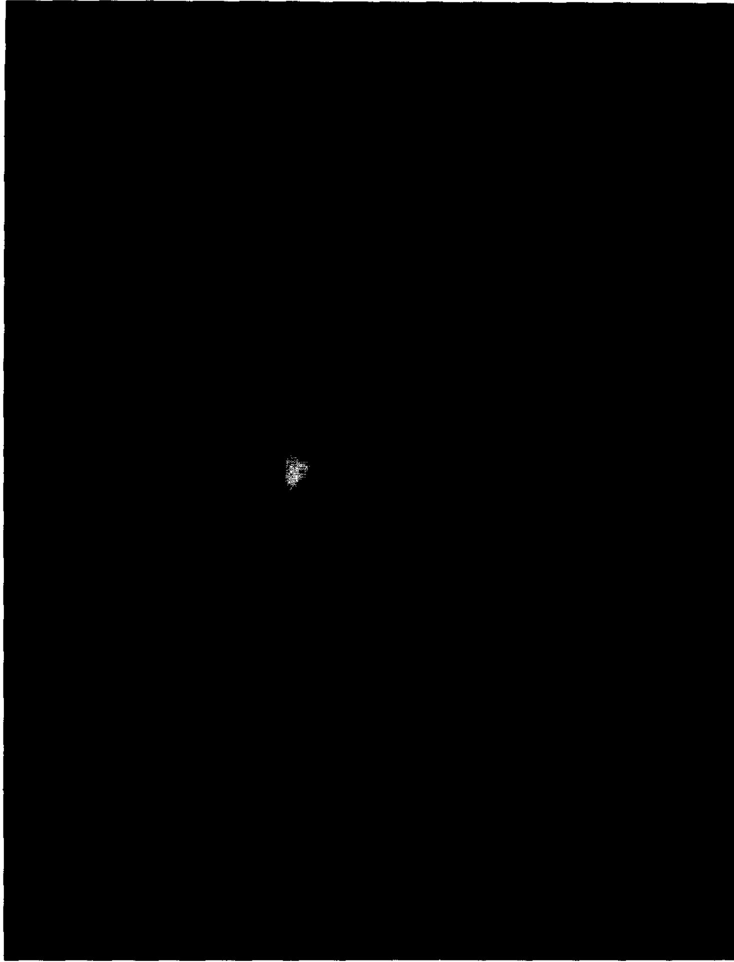

Fig. 12. Section of a copper ball with a void in it, discharge in air, $R_w = 0.8$ mm, $p = 1.8$ mmHg, 0.9999 copper anode.

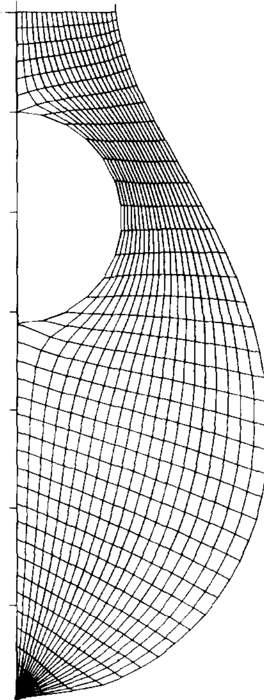

Fig. 13. The body-fitted coordinate system corresponding to Fig. 12 generated by equations (54) and (55) of Part I [4].

REFERENCES

1. I. M. Cohen, K. Ramakrishna and P. S. Ayyaswamy, An experimental study of ball formation processes with aluminum and copper, *Expl Thermal Fluid Sci.* **2,** 57–64 (1989).
2. L. J. Huang, K. M. Yu, S. Powell, I. M. Cohen and P. S. Ayyaswamy, Ball formation in wire bonding—I. Upscaled experimental study, *Int. J. Hybrid Microelectron.* **13,** 1–5 (1990).
3. I. M. Cohen and P. S. Ayyaswamy, Ball formation processes in aluminum bonding wire, *Solid State Technol.* **28,** 89–95 (December 1985).
4. L. J. Huang, P. S. Ayyaswamy and I. M. Cohen, Melting and solidification of thin wires: a class of phase-change problems with a mobile interface—I. Analysis. *Int. J. Heat Mass Transfer* **38,** 1637–1645 (1995).
5. L. J. Huang, K. Ramakrishna, P. S. Ayyaswamy and I. M. Cohen, An analysis of solidification of metals and alloys accompanied by density change and void formation, *ASME J. Electron. Packaging* **111,** 119–206 (1989).